Monthly Notices of the ROYAL ASTRONOMICAL SOCIETY

MNRAS **526,** 263–278 (2023) https://doi.org/10.1093/mnras/stad2704
Advance Access publication 2023 September 08

Stratospheric dayside-to-nightside circulation drives the 3D ozone distribution on synchronously rotating rocky exoplanets

Marrick Braam [1,2,3]★ Paul I. Palmer,[1,2] Leen Decin,[3] Maureen Cohen[1,2] and Nathan J. Mayne[4]

[1]*School of GeoSciences, University of Edinburgh, Edinburgh EH9 3FF, UK*
[2]*Centre for Exoplanet Science, University of Edinburgh, Edinburgh EH9 3FD, UK*
[3]*Institute of Astronomy, KU Leuven, B-3001 Leuven, Belgium*
[4]*Department of Physics and Astronomy, Faculty of Environment Science and Economy, University of Exeter, Exeter EX4 4QL, UK*

Accepted 2023 August 17. Received 2023 August 12; in original form 2023 June 5

ABSTRACT

Determining the habitability and interpreting future atmospheric observations of exoplanets requires understanding the atmospheric dynamics and chemistry from a 3D perspective. Previous studies have shown significant spatial variability in the ozone layer of synchronously rotating M-dwarf planets, assuming an Earth-like initial atmospheric composition. We simulate Proxima Centauri b in an 11.2-d orbit around its M-type host star using a 3D coupled climate-chemistry model to understand the spatial variability of ozone and identify the mechanism responsible for it. We document a previously unreported connection between the ozone production regions on the photochemically active dayside hemisphere and the nightside devoid of stellar radiation and thus photochemistry. We find that stratospheric dayside-to-nightside overturning circulation can advect ozone-rich air to the nightside. On the nightside, ozone-rich air subsides at the locations of two quasi-stationary Rossby gyres, resulting in an exchange between the stratosphere and troposphere and the accumulation of ozone at the gyre locations. The mechanism drives the ozone distribution for both the present atmospheric level (PAL) and a 0.01 PAL O_2 atmosphere. We identify the hemispheric contrast in radiative heating and cooling as the main driver of the stratospheric dayside-to-nightside circulation. An age-of-air experiment shows that the mechanism also impacts other tracer species in the atmosphere (gaseous and non-gaseous phase) as long as chemical lifetimes exceed dynamical lifetimes. These findings, applicable to exoplanets in similar orbital configurations, illustrate the 3D nature of planetary atmospheres and the spatial and temporal variability that we can expect to impact spectroscopic observations of exoplanet atmospheres.

Key words: planets and satellites: atmospheres – planets and satellites: composition – planets and satellites: terrestrial planets.

1 INTRODUCTION

The past two decades have seen the discovery of numerous Earth-size exoplanets, with a substantial fraction of them orbiting in the circumstellar Habitable Zone (Kasting, Whitmire & Reynolds 1993). Earth-size planets are preferentially discovered around M-dwarf stars (Dressing & Charbonneau 2015), because they are the most abundant stellar type, have relatively small radii, and are relatively cool, allowing for exoplanets in short-period orbits. The habitability of such exoplanets has been debated in light of the stellar and planetary environments (Shields, Ballard & Johnson 2016). Comprehensive numerical simulations that describe the physical and chemical properties of a planetary atmosphere in such environments are essential to understanding habitability and interpreting spectroscopic observations.

Since M stars are cooler and smaller than other stellar types, a planet in the Habitable Zone orbits at a small orbital distance and feels a strong gravitational pull from the host star. This can lead to spin-orbit resonances for the planet, so-called tidal locking, of which the most extreme case is the 1:1 resonant orbit or synchronous rotation (e.g. Barnes 2017; Renaud et al. 2021). Simulations with General Circulation Models (GCMs) help us understand how synchronous rotation affects the planetary atmosphere and surface habitability. First, synchronous rotation creates distinct hemispheric environments and a large temperature difference between the dayside and nightside (e.g. Joshi, Haberle & Reynolds 1997). Secondly, synchronous rotation leads to distinct photochemical environments, with strong photochemical production and destruction on the dayside and an absence of photochemistry on the nightside (e.g. Proedrou & Hocke 2016; Chen et al. 2018; Yates et al. 2020; Braam et al. 2022; Ridgway et al. 2023). Depending on the rotation period, synchronous rotation can also lead to atmospheric circulation that is characterized by thermally direct circulation for slowly rotating planets (e.g. Merlis & Schneider 2010; Edson et al. 2011; Heng, Frierson & Phillipps 2011; Koll & Abbot 2016; Haqq-Misra et al. 2018). The existence of this large-scale circulation requires the Rossby deformation radius to exceed the planetary radius (Carone, Keppens & Decin 2014, 2015; Noda et al. 2017; Haqq-Misra et al. 2018), which is the case for planets like Proxima Centauri b, Trappist-1 e to h, LHS-1140 b, and GJ 667 C c, assuming an Earth-like atmosphere. The dayside–nightside contrast leads to an overturning

★ E-mail: mbraam@ed.ac.uk

circulation, with upwelling on the dayside and downwelling on the nightside (Showman et al. 2013). This vertical motion results in a superposition of planetary-scale Rossby and Kelvin waves, which drives eddy momentum equatorward (Showman & Polvani 2010). A typical part of this wave structure is a pair of quasi-stationary cyclonic gyres on the nightside (Showman & Polvani 2010). The equatorward momentum feeds the superrotating jet (Showman & Polvani 2011). The overturning circulation is a dominant component of the dayside-to-nightside heat transport (Hammond & Lewis 2021).

Atmospheric circulation impacts the spatial and temporal distribution of chemical species and other tracers such as clouds (e.g. Boutle et al. 2017; Komacek & Abbot 2019; Sergeev et al. 2020) and photochemical hazes (Parmentier, Showman & Lian 2013; Steinrueck et al. 2021). On Earth, the Brewer–Dobson circulation controls the large-scale distribution of chemical tracers such as ozone (O_3) and water vapour in the atmosphere (Butchart 2014). Ozone formation is initiated by photochemistry through the Chapman mechanism (Chapman 1930), which is strongest at tropical latitudes. The Brewer–Dobson circulation describes the ascent of ozone-rich air in the tropics, followed by equator-to-pole transport and descending air motions at high latitudes, leading to meridional variations with a relatively enhanced ozone layer at high latitudes. The production of ozone depends on the presence of molecular oxygen, which has been at a mole fraction of $\chi_{O_2} = 21$ per cent for the past ∼0.5 Gyr but was substantially less abundant for most of Earth's history (e.g. Lyons, Reinhard & Planavsky 2014). Oxygen levels during the Proterozoic (2.4–0.54 Gyr ago) were likely between 0.01 and 0.001 times the present atmospheric level (PAL; Lyons et al. 2014; Cooke et al. 2022). Decreasing oxygen levels down to 0.001 PAL leads to a thinner ozone layer, from a present-day global average ozone column density of 279 DU (DU: 1 DU = 2.687×10^{20} molecules m^{-2}) to 66 DU for a 0.01 PAL case (Cooke et al. 2022). Nevertheless, the Brewer–Dobson circulation and the associated meridional variability seem to persist (see fig. 4 in Cooke et al. 2022).

Proedrou & Hocke (2016) simulated a tidally locked Earth using a 3D climate-chemistry model (CCM), which consists of a GCM coupled to a photochemical network to study the relation between (photo)chemistry, atmospheric dynamics and the thermal structure of the atmosphere. They find a breakdown of the Brewer–Dobson circulation, and instead predict that ozone accumulates on the nightside, where it has a long lifetime (Proedrou & Hocke 2016). Carone et al. (2018) investigated stratospheric circulation on tidally locked exoplanets and the potential impact on the distribution of chemical species. For planets with short orbital periods (<25 d), tropical Rossby waves can induce strong equatorial jets in the stratosphere with pole-to-equator transport of airmasses (Carone et al. 2018). Chen et al. (2019) showed the meridional distribution of ozone from CCM simulations, confirming that this pole-to-equator circulation essentially confines photochemical species such as ozone to the equatorial regions. The existence of extratropical Rossby waves or damping of tropical Rossby waves prevents this equatorial confinement. Instead, a thermally driven overturning circulation can drive equator-to-pole transport of photochemical species (Carone et al. 2018; Chen et al. 2019), leading to meridional structure with enhanced ozone at high latitudes. For planets like Proxima Centauri b, Carone et al. (2018) find a relatively weak tropical Rossby wave, with a thermally driven equator-to-pole circulation existing in the stratosphere (see their fig. 12). For such planets, the enhanced ozone abundances at high latitudes were later also simulated by Chen et al. (2019).

The distribution of radiatively active species such as ozone impacts habitability (e.g. Ridgway et al. 2023), and will determine what spectroscopic observations of the planetary atmosphere will look like. For hot Jupiters, dayside–nightside variations in temperature and chemical abundances (Nixon & Madhusudhan 2022; Pluriel 2023) and 3D transport-induced quenching (Zamyatina et al. 2023) both affect the appearance of synthetic spectra. For rocky planets, the spatial and temporal variation of water clouds causes variability in observations (May et al. 2021; Cohen et al. 2023). Moreover, spatial and temporal variability of gaseous chemical species can manifest itself in spectroscopic variations over the orbital phase or observing geometry (Cooke et al. 2023). Despite reporting a non-detection for the atmosphere, the observation of TRAPPIST-1 b illustrates the capability of *JWST* to characterize Earth-size exoplanets (Greene et al. 2023).

For the exoplanets that have an atmosphere, we need to understand their 3D nature, including circulation, clouds, and atmospheric chemistry, which motivates the application of 3D CCMs to exoplanetary environments. Such simulations of synchronously rotating exoplanets predict a significant zonal structure in the ozone layer for planets around M-dwarfs like Proxima Centauri b (Yates et al. 2020; Braam et al. 2022) and haze distribution for hot Jupiters (Parmentier et al. 2013; Steinrueck et al. 2021). Yates et al. (2020) found that ozone has a much longer chemical lifetime on the nightside as compared to the dayside of M-dwarf exoplanets. These long nightside lifetimes lead to the accumulation of ozone in the nightside gyres, despite the absence of stellar radiation needed to initiate the relevant photochemistry. This spatially variable ozone layer indicates a connection between the photochemically active dayside regions and nightside gyres, which is currently not understood.

In this paper, we aim to understand the dayside–nightside connection and identify the physical and chemical mechanism that drives the spatially variable ozone layer on synchronously rotating exoplanets around M-dwarf stars. We use a 3D CCM to investigate the spatial and temporal structure of atmospheric ozone, in a configuration for Proxima Centauri b. In Section 2, we briefly describe the CCM and introduce metrics used to diagnose atmospheric circulation. This will be followed by a description of the ozone distribution and its relation to atmospheric circulation in Section 3, mainly focusing on 1 PAL O_2 and then testing the mechanism for a 0.01 PAL O_2 atmosphere. In Section 4, we identify a possible driver of the circulation, investigate variability in our simulations and discuss the potential observability. Finally, we present the conclusions of our study in Section 5.

2 METHODS

This section starts with a description of the 3D CCM. This is followed by the introduction of useful metrics to diagnose atmospheric circulation and its impact on chemistry in Section 2.2. Finally, we summarize the experimental set-up in Section 2.3.

2.1 Coupled Climate-Chemistry Model

The 3D CCM consists of the Met Office Unified Model (UM) as the GCM coupled with the UK Chemistry and Aerosol framework (UKCA), in the configuration described by Braam et al. (2022). UM-UKCA is used to simulate the atmospheric dynamics and chemistry for Proxima Centauri b, but the results apply to other planets in similar orbits around M-dwarf stars. We simulate an aquaplanet with 1 bar or 1000 hPa surface pressure (see Braam et al. 2022, and references therein) and use a horizontal resolution of 2° by 2.5° in latitude and longitude, respectively. The atmosphere extends up to

Table 1. Orbital and planetary parameters for the Proxima Centauri b set-up, following Boutle et al. (2017).

Parameter	Value
Semimajor axis (au)	0.0485
Stellar irradiance (W m^{-2})	881.7
Orbital period (d)	11.186
Rotation rate (rad s^{-1})	6.501×10^{-6}
Eccentricity	0
Obliquity	0
Radius ($R_\oplus$)	1.1
Surface gravity (m s^{-2})	10.9

85 km in 60 vertical levels. We assume that Proxima Centauri b is in a 1:1 resonant orbit around its M-dwarf host star and use the orbital parameters as shown in Table 1. The substellar point is located at 0° latitude (ϕ) and 0° longitude (λ).

The UM is used in the Global Atmosphere 7.0 configuration (Walters et al. 2019), including the ENDGame dynamical core to solve the non-hydrostatic fully compressible deep-atmosphere equations of motion (Wood et al. 2014). Parametrized sub-grid processes include convection (mass-flux approach, based on Gregory & Rowntree 1990), water cloud physics (Wilson et al. 2008), turbulent mixing (Lock et al. 2000; Brown et al. 2008), and the generation of lightning (Price & Rind 1992; Luhar et al. 2021; Braam et al. 2022). The incoming stellar radiation for 0.5 nm to 5.5 μm is described by the v2.2 composite spectrum for Proxima Centauri from the MUSCLES spectral survey (France et al. 2016; Loyd et al. 2016; Youngblood et al. 2016) and extended to 10 μm using the spectrum from Ribas et al. (2017). Radiative transfer through the atmosphere is treated by the Suite of Community Radiative Transfer codes based on Edwards and Slingo (SOCRATES) scheme (Edwards & Slingo 1996). The UM is one of the leading models in predicting the Earth's weather and climate and has been adapted for the study of several types of exoplanets, including terrestrial planets (e.g. Mayne et al. 2014a; Boutle et al. 2017; Lewis et al. 2018; Eager et al. 2020; Yates et al. 2020; Braam et al. 2022; Ridgway et al. 2023) but also Mini-Neptunes (e.g. Drummond et al. 2018a) and hot Jupiters (e.g. Mayne et al. 2014b, 2017). Furthermore, the UM was part of the TRAPPIST-1e Habitable Atmosphere Intercomparison project (Fauchez et al. 2021, 2022; Sergeev et al. 2022a; Turbet et al. 2022).

We use UKCA to simulate the 3D atmospheric chemical composition, by including its description of gas-phase chemistry. UKCA is fully coupled to the UM for large-scale advection, convective transport and boundary layer mixing of the chemical tracers (Morgenstern et al. 2009; O'Connor et al. 2014; Archibald et al. 2020). The Fast-JX photolysis scheme is implemented within UKCA, to calculate photolysis rates of chemical species in the atmosphere (Wild, Zhu & Prather 2000; Bian & Prather 2002; Neu, Prather & Penner 2007; Telford et al. 2013). By taking into account the varying optical depths of Rayleigh scattering, absorbing gases, and clouds from the UM, Fast-JX provides an interactive treatment of photolysis in calculating the 3D distribution of chemical species in the atmosphere. We distribute the stellar flux from Proxima Centauri over the 18 wavelength bins of Fast-JX, as shown in Braam et al. (2022) and their fig. 1. These fluxes are synchronized to the orbital distance of Proxima Centauri b which provides an interactive calculation of photolysis rates over the planetary orbit. The chemistry included is a reduced version of UKCA's Stratospheric–Tropospheric scheme (StratTrop; Archibald et al. 2020), including the Chapman mechanism of ozone formation, and the hydrogen oxide ($HO_x = H + OH + HO_2$) and nitrogen oxide ($NO_x = NO + NO_2$) catalytic cycles. This results in 21 chemical species that are connected by 71 reactions, describing the main mechanisms that control the abundance of ozone in an Earth-like atmospheric composition. A full list of species and reactions can be found in the appendix of Braam et al. (2022).

2.2 Metrics

The meridional circulation is diagnosed using the mean meridional mass streamfunction (in kg s^{-1}), which calculates the northward mass flux above pressure P:

$$\Psi_\mathrm{m} = \frac{2\pi R_\mathrm{p} \cos\phi}{g} \int_0^P \bar{v}\,\mathrm{d}P, \tag{1}$$

with R_p as the planetary radius, g as the gravitational acceleration, and $\bar{v}$ as the zonal and temporal mean of the northward velocity component at latitude ϕ. Earlier studies using this metric for synchronously rotating exoplanets (e.g. Merlis & Schneider 2010; Edson et al. 2011; Carone, Keppens & Decin 2015; Haqq-Misra & Kopparapu 2015; Carone et al. 2018) showed (1) the existence of tropospheric Hadley and Ferrel cells transporting heat and mass from the equatorial to polar regions and (2) the impact of orbital configuration on the Brewer–Dobson circulation in the stratosphere (Carone et al. 2018).

However, with the fixed substellar point of synchronously rotating planets, the mean meridional circulation varies depending on the position relative to the substellar point: for example, the hemispheric mean meridional circulation can vary significantly between the dayside and nightside. The zonal circulation is analogous to the Walker circulation cells on Earth, with rising motion at the location of the heat source, followed by eastward and westward flow aloft and, after descending on the nightside, a return flow along the surface back to the heat source (Geisler 1981). The mean zonal mass streamfunction can be used to calculate the eastward mass flux above pressure P:

$$\Psi_z = \frac{2\pi R_\mathrm{p}}{g} \int_0^P \bar{u}\,\mathrm{d}P, \tag{2}$$

where $\bar{u}$ is the meridional mean of the zonal velocity component. For slow rotators, the mean zonal circulation connects the substellar and antistellar points (Gill 1980; Merlis & Schneider 2010; Edson et al. 2011; Heng et al. 2011; Showman & Polvani 2011; Haqq-Misra & Kopparapu 2015; Haqq-Misra et al. 2018). The substellar–antistellar circulation also consists of a cross-polar flow (Haqq-Misra & Kopparapu 2015).

As elaborated in Section 1, the total wind flow on synchronously rotating exoplanets consists of several components. We perform a Helmholtz decomposition of the total wind flow, following Hammond & Lewis (2021). This decomposes the total wind flow into its rotational, eddy rotational, and divergent components. The divergent wind mainly drives the substellar–antistellar overturning circulation (Hammond & Lewis 2021; Sergeev et al. 2022a). Since the divergent component is roughly isotropic around the substellar point, we can move from the usual latitude–longitude or geographic coordinate system to a tidally locked coordinate system (Koll & Abbot 2015; Hammond & Lewis 2021). The transformation between geographic coordinates and tidally locked coordinates is illustrated in Fig. 1. The tidally locked latitude ϕ' is measured as the angle from the terminator (at $\phi' = 0$, see Fig. 1b) and the tidally locked longitude λ' is the angle about the substellar point (see Fig. 1c), with the geographic North Pole located at $(\phi', \lambda') = (0, 0)$ in tidally locked coordinates. The substellar point and antistellar point correspond to

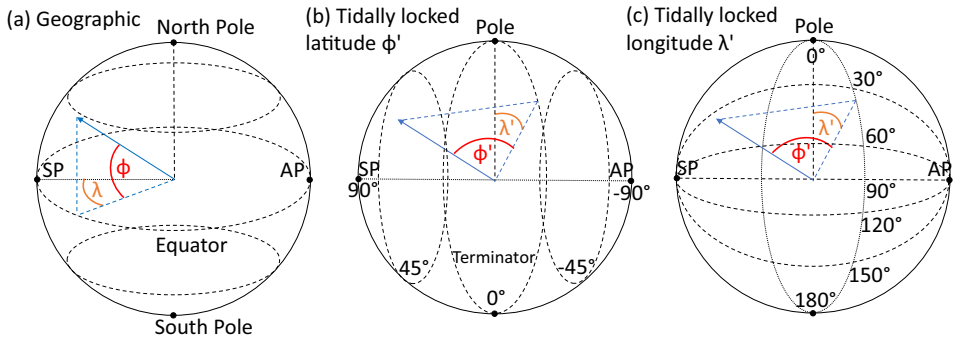

Figure 1. Geographic coordinate system (a) showing latitude ϕ and longitude λ, with the substellar point (SP) located at (0°, 0°). In the tidally locked coordinate system, we use tidally locked latitude ϕ' and tidally locked longitude λ'. Panel (b) illustrates tidally locked latitudes, with the substellar point located at $\phi' = 90°$, the terminator at $\phi' = 0°$, and the nightside corresponding to negative ϕ'. Panel (c) shows tidally locked longitudes, illustrating how lines of constant tidally locked longitude connect the substellar and antistellar (AP) points. Figures based on Koll & Abbot (2015).

$\phi' = 90°$ and $-90°$, respectively. In representing a sphere on a 2D plot, the geographic coordinate system stretches the poles and thereby emphasizes meridional gradients (e.g. equator-to-pole temperature gradients). Meridional gradients are especially pronounced when the axial rotation is substantially faster than the orbital rotation. For synchronously rotating planets, the rotation periods are the same, giving the strongest gradients between the substellar and antistellar points. Therefore, the tidally locked coordinate system stretches the substellar and antistellar points as the extrema in ϕ'. As illustrated in Fig. 1(c), every line of constant λ' corresponds to a line connecting the substellar point and antistellar point, in every direction over the sphere. Hence, cross-polar flow in geographic coordinates is automatically taken into account in the tidally locked coordinate system and was found to be an important contribution to the tropospheric dayside-to-nightside circulation (Hammond & Lewis 2021). It was shown by Hammond & Lewis (2021) that integrating the continuity equation in tidally locked coordinates over λ' leads to the tidally locked mean meridional mass streamfunction:

$$\Psi'_{\rm m} = \frac{2\pi R_{\rm p} \cos\phi'}{g} \int_0^P \bar{v}' {\rm d}P, \tag{3}$$

where $\bar{v}'$ is the zonal mean of the meridional velocity component at tidally locked latitude ϕ'. In this system, the meridional mass streamfunction calculates the mass flux towards the antistellar point (along lines of constant λ'), connecting the substellar and antistellar points while covering the whole planet.

Since we are particularly interested in the transport of ozone around the planet, we weight the streamfunctions using the ozone mass mixing ratio (MMR), which is measured as the mass of ozone per unit mass of air in a parcel. This gives us the ozone mass streamfunction:

$$\Psi'_{\rm m,O_3} = \Psi'_{\rm m} \times {\rm MMR}_{\rm O_3}, \tag{4}$$

which can be applied generally using any of the streamfunctions in equations (1), (2), or (3) to give the ozone-weighted meridional, zonal, or the tidally locked meridional mass streamfunction.

In assessing the impact of atmospheric dynamics on chemical abundances, it is important to make a comparison between the time-scales of processes that can control the ozone abundance. The dynamical lifetimes include the zonal (τ_u), meridional (τ_v), and vertical components (τ_w), and are calculated following Drummond et al. (2018b):

$$\tau_u = \frac{L}{u} = \frac{2\pi R_{\rm p}}{u}, \tag{5}$$

$$\tau_v = \frac{L}{v} = \frac{\pi R_{\rm p}}{v}, \tag{6}$$

$$\tau_w = \frac{H}{w}, \tag{7}$$

with L the relevant horizontal scale in terms of the planetary radius $R_{\rm p}$ and H the vertical scale height. The zonal (u), meridional (v), and vertical (w) wind components are all in m s^{-1}. For the chemical lifetimes we use

$$\tau_{\rm chem} = \frac{n_{\rm O_3}}{R_x}, \tag{8}$$

where $n_{\rm O_3}$ denotes the ozone number density (molecules m^{-3}) and R_x the loss of ozone (in molecules m^{-3} s^{-1}) due to reaction x. Specifically, we use the termination reaction of the Chapman mechanism (Chapman 1930; Braam et al. 2022):

$$\rm O_3 + O(^3P) \longrightarrow O_2 + O_2, \qquad (R1)$$

and the rate-limiting step of the dominant HO$_x$ catalytic cycle (Yates et al. 2020; Braam et al. 2022):

$$\rm HO_2 + O_3 \longrightarrow OH + 2O_2. \qquad (R2)$$

A detailed overview of the chemical reactions can be found in Braam et al. (2022). We calculate the lifetimes for sets of grid-points centred at four distinct locations in the ozone distribution (see Fig. 3), and subsequently take the meridional and zonal mean. These locations cover the substellar point (10 latitudes × 8 longitudes = 80 grid points), the nightside jet (10 × 7 = 70 points), and the two nightside gyres with 5 × 7 = 35 points each.

2.3 Experimental set-up

We use the final state of the 'Chapman + HO$_x$ + NO$_x$' simulation from Braam et al. (2022) for the analysis. The atmosphere was initialized at an Earth-like atmospheric composition, using pre-industrial values of N_2, O_2, and CO_2 (see also Boutle et al. 2017). Water vapour profiles are interactively determined by evaporation from the slab ocean. The HO$_x$ and NO$_x$ species are initialized at MMRs of 10^{-9} and 10^{-15}, respectively. To test our results for an atmosphere of lower oxygen content, we initialize a second simulation with 0.01 PAL O_2 and an increased amount of N_2 to

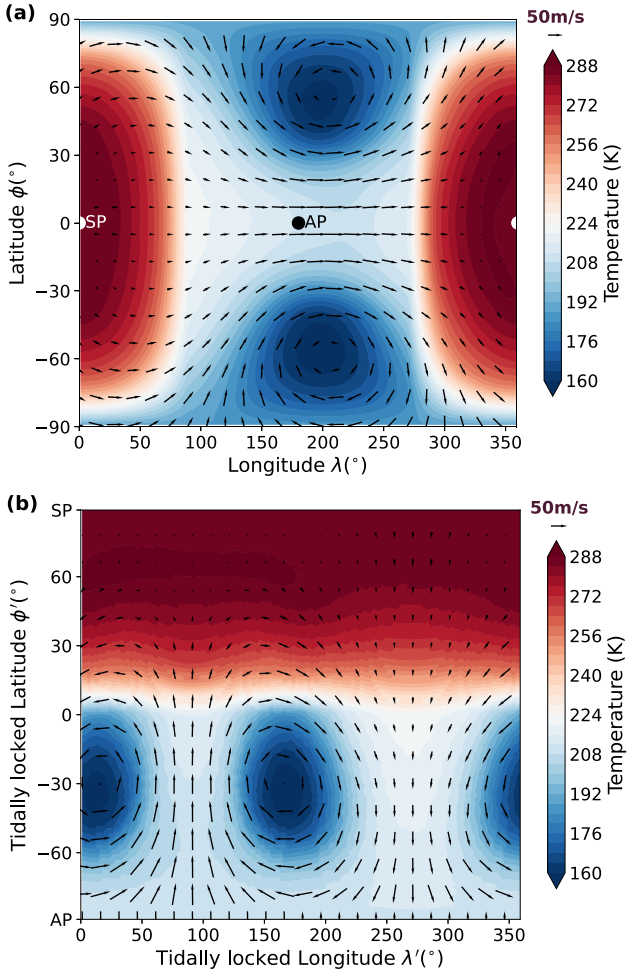

Figure 2. Temporal mean surface temperature over 50 orbits of Proxima Centauri b, using (a) the geographic coordinate system and (b) the tidally locked coordinate system (Koll & Abbot 2015). The substellar point (SP) is transformed from $(\phi, \lambda) = (0^\circ, 0^\circ)$ in geographic coordinates (white dot) to $\phi' = 90^\circ$ in tidally locked coordinates, as also shown in Fig. 1. Overplotted are the horizontal wind vectors at $P \approx 400$ hPa, showing both the tropospheric jet and the existence of the Rossby gyres on the nightside. The plots also show the location of the antistellar point (AP).

maintain a surface pressure of 1000 hPa. This decrease in oxygen is informed by the fact that for most of Earth's history, the atmosphere contained lower O_2 levels than we presently see (Lyons et al. 2014).

We report results from our simulations as 600-d mean of the CCM output (equal to ∼50 orbits of Proxima Centauri b) after spinning up to ensure the simulations have reached a dynamical and chemical steady state. The dynamical steady state was determined by the stabilization of the surface temperature and radiative balance at the top of the atmosphere. The chemical steady state was determined by the stabilization of ozone as a long-lived species, through the total column density and mole fraction χ_{O_3}. In diagnosing the impact of dynamical processes on the ozone distribution, parts of the spin-up period have also been used to plot the evolution of chemically inert tracers (see e.g. Fig. 7 below). The analysis of temporal variability in Section 4.3 is based on a 6-d output over 900 d of simulation after reaching a steady state, to ensure we include potential variability at longer time-scales.

3 RESULTS

In this section, we start with a brief description of the planetary climate and ozone layer, focusing on the 1 PAL O_2 atmosphere. After that, we discuss the atmospheric circulation followed by its impact on the distribution of ozone around the planet, elaborating on the stratospheric overturning circulation. We then perform a comparison of relevant lifetimes in the atmosphere and investigate the implications of the stratospheric overturning circulation for lightning-induced chemistry. We end with testing how a 0.01 PAL O_2 atmosphere affects the stratospheric overturning circulation and ozone distribution.

3.1 Planetary climate and atmospheric ozone

The simulated climate of Proxima Centauri b is broadly similar to that described by Boutle et al. (2017). Furthermore, the formation of an ozone layer under quiescent stellar radiation is explained in detail by Yates et al. (2020) and Braam et al. (2022). Here, we give a brief description of the details essential for this study. The simulated surface temperature of Proxima Centauri b is shown in Fig. 2, using a geographic coordinate system in panel (a) and a tidally locked coordinate system in panel (b). Both panels show the dayside-to-nightside contrast characteristic of synchronous rotation, with dayside maxima in surface temperature of up to 289 K and minima of 157 K over the nightside Rossby gyres. Fig. 2(b) demonstrates the usefulness of the tidally locked coordinate system in identifying the dayside-to-nightside contrasts, with the terminator located at $\phi' = 0^\circ$. The horizontal wind vectors are shown at $P \approx 400$ hPa, illustrating the tropospheric jet as well as the Rossby gyres on the nightside. The dayside-to-nightside circulation is part of an overturning circulation across multiple pressure levels that will be described in more detail in Section 3.2. At the locations of the nightside Rossby gyres (Showman & Polvani 2010), we see the coldest areas on the planetary surface with air that is trapped and subject to radiative cooling. The atmospheric pressure in the gyres is relatively low, like the eye of tropical cyclones (Schubert et al. 2007). The gyres are relatively isolated from the rest of the hemisphere and their edges act as mixing barriers (Vallis 2017). The gyres are a general feature of slowly rotating exoplanets in a synchronous orbit with a single equatorial jet in the troposphere (Sergeev et al. 2022b).

We find a spatially variable distribution of ozone in Fig. 3(a), with a relatively thin dayside ozone layer and accumulation of ozone on the nightside. Typical values for the vertically integrated ozone column densities on Earth are 200–400 DU, with lower values over the equatorial regions and ozone hole and higher values over high-latitude regions (Eyring et al. 2013). For synchronously rotating planets, most of the dayside ozone column density falls within this range. The locations of the nightside Rossby gyres correspond to the maxima in the thickness of the ozone column, reaching up to 1401 DU. The gyres are not fully symmetric, evident from slightly different shapes and the average ozone columns: the area-weighted mean column density of the low-λ' gyre (for $\lambda' \leq 70$ and $\lambda' > 320^\circ$) is equal to 626 DU and of the mid-λ' gyre ($110 < \lambda' \leq 220^\circ$) to 601 DU, both confined between tidally locked latitudes $-60 < \phi' < 0^\circ$. Fig. 3(b) shows that the accumulation of ozone at the gyre locations mostly occurs in the lower atmosphere, at pressure levels corresponding to the troposphere (<100 hPa). The highest χ_{O_3} are found between 10 and 0.1 hPa and form a significant contribution to the planetary ozone layer, especially on the dayside.

The existence of such a spatially variable ozone layer depends on a complex interplay between photochemistry and atmospheric

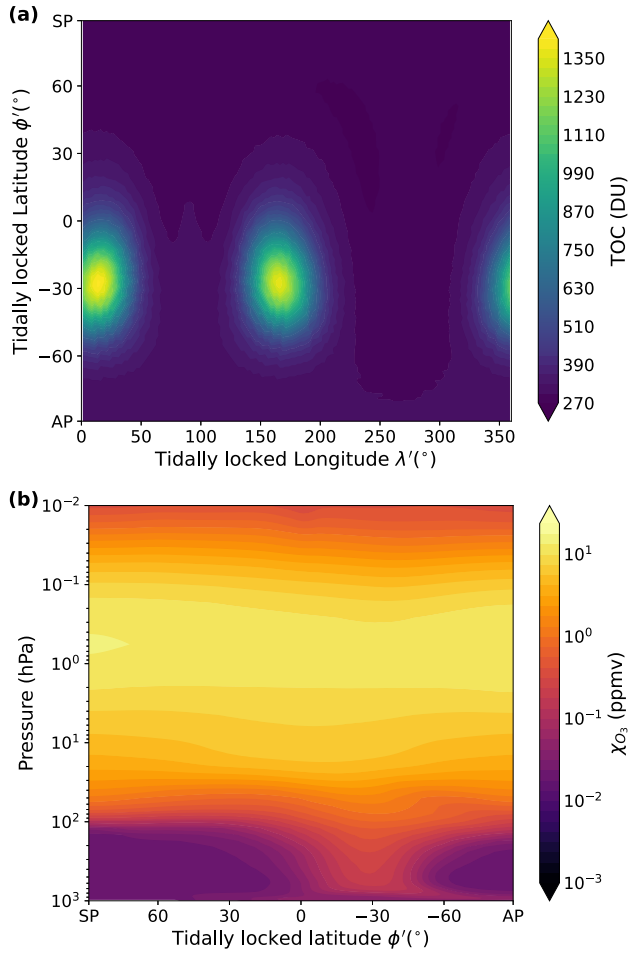

Figure 3. (a) Total ozone column density and (b) mole fraction χ_{O_3}, both taking means over 50 orbits of Proxima Centauri b. Both plots illustrate the spatially variable ozone layer with accumulation at the locations of the nightside Rossby gyres ($-60 < \phi' < 0$). The substellar and antistellar point are denoted as SP and AP, respectively.

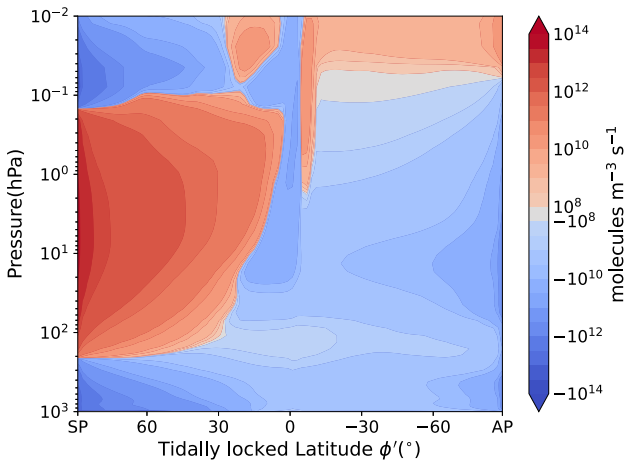

Figure 4. Meridional mean ozone chemical tendency (the balance between chemical production and loss) in tidally locked coordinates, showing that ozone production is limited to the planet's dayside.

dynamics and changes as a function of incoming stellar radiation and planetary rotation state (Chen et al. 2019, 2021). The production mechanisms for atmospheric ozone are relatively well understood and due to photochemistry: in the presence of stellar radiation molecular oxygen will dissociate and form ozone through the Chapman mechanism (Chapman 1930). The 3D impact of M-dwarf radiation on the Chapman mechanism has been explored by previous studies, both in quiescent (Yates et al. 2020; Braam et al. 2022) and flaring conditions (Ridgway et al. 2023). In all cases, an ozone layer develops around the planet. As such exoplanets are likely to rotate synchronously around their host star (Barnes 2017), stellar radiation and the photochemical production of ozone are limited to the planetary dayside. This is illustrated in Fig. 4, showing the time-averaged chemical tendency of ozone. The tendency denotes the balance between the production and loss of ozone due to chemical processes. We find that ozone production mainly occurs on the dayside and is particularly strong at high $\phi' > 45^\circ$ (i.e. close to the substellar point), whereas ozone production is practically absent at the locations of the nightside gyres ($-60 < \phi' < 0^\circ$) and more generally the nightside troposphere (below ∼100 hPa) and stratosphere (between ∼100 and 0.1 hPa). Hence, another mechanism must be driving the relatively enhanced ozone abundances at the locations of the nightside Rossby gyres. In the upper atmosphere (above ∼0.1 hPa), atomic oxygen is quickly advected to the nightside where it forms ozone and thus gives net ozone production. The ozone is subsequently advected back to the dayside, where it is destroyed by the photochemical loss processes that are particularly strong in these top layers of the atmosphere.

3.2 Overturning circulations

The relationship between the ozone distribution in Fig. 3 and the global atmospheric circulation becomes clear through the mass streamfunctions, as defined in Section 2.2. From left to right, Fig. 5 shows the mean meridional mass streamfunctions Ψ_m, Ψ'_m, and Ψ'_{m,O_3} that have been calculated from the divergent wind component. A positive streamfunction (red contours) indicates clockwise circulation, and a negative streamfunction (blue) indicates anticlockwise circulation.

From Fig. 5(a), we find strong poleward transport of air at tropospheric pressures (>100 hPa) in a single thermally driven circulation cell (Merlis & Schneider 2010; Edson et al. 2011). Moving up into the stratosphere, we find stacked layers of clockwise and anticlockwise circulation. The existence of poleward transport between ∼50 and ∼1.5 hPa indicates additional thermally driven circulation cells. These cells transport aerosols and chemical tracers such as ozone from the equator to the poles through the stratosphere (Carone et al. 2018; Chen et al. 2019). This equator-to-pole transport leads to an enhanced high latitude ozone layer on the dayside in geographic coordinates, with mean ozone column densities of ∼490 DU above 80° North and South as compared to a mean of ∼290 DU between 10° North and 10° South (see also Yates et al. 2020; Braam et al. 2022). Since the stellar radiation at the poles is too weak to initiate the photochemistry responsible for ozone production, this polar enhancement has to be due to the poleward transport of ozone produced in the equatorial regions.

Moving to tidally locked coordinates using Ψ'_m in Fig. 5(b), we find a single overturning circulation cell that dominates the troposphere and transports air and heat from the dayside towards the nightside. A weaker anticlockwise circulating cell is present between the antistellar point and $\phi' \approx -30^\circ$, induced by the temperature gradient between those two points. The absence of anticlockwise

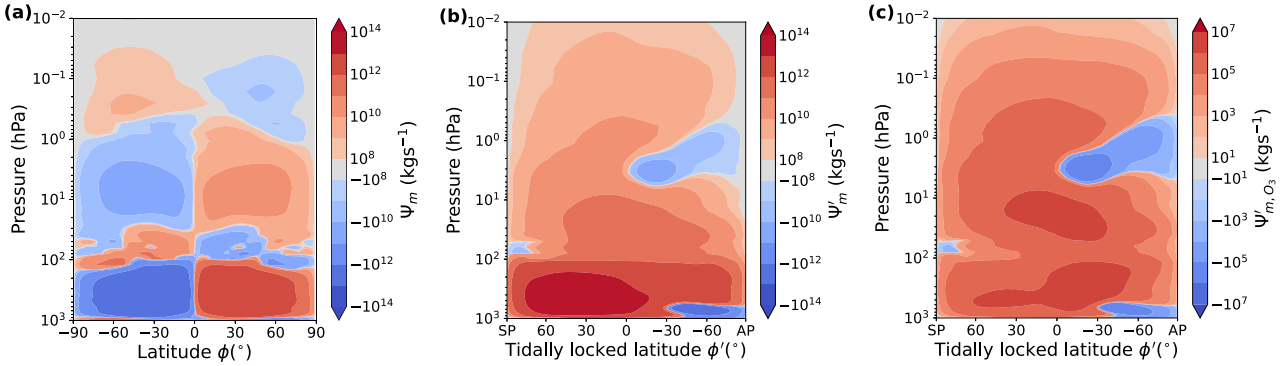

Figure 5. Zonal mean meridional mass streamfunctions illustrating different aspects of atmospheric circulation. Positive values (red) indicate clockwise and negative values (blue) anticlockwise motion. (a) The meridional mass streamfunction in geographic coordinates Ψ_m (equation 1) shows equator-to-pole stratospheric transport like the Brewer–Dobson circulation. (b) The meridional mass streamfunction in tidally locked coordinates Ψ'_m (equation 3) shows an overturning dayside-to-nightside circulation including a strong stratospheric component (above ∼100 hPa). (c) The meridional ozone mass streamfunction Ψ'_{m,O_3} (equation 4) shows that this stratospheric component is significant in terms of transporting ozone from the dayside to the nightside.

motion when moving to lower pressure levels in Fig. 5(b) indicates that a connection between the tropospheric cell and the stratospheric circulation exists. An overturning circulation covers essentially all of the stratosphere, connecting the dayside and nightside. Air ascends in the ozone production regions (between 0.2 and 100 hPa; see Fig. 4) and moves through the stratosphere towards the nightside, where it subsides at the locations of the nightside gyres and thus the locations of ozone accumulation as shown in Fig. 3.

To quantify the impact of this mass transport on the distribution of ozone, we calculate the tidally locked ozone-weighted mass streamfunction Ψ'_{m,O_3} (equation 4) as shown in Fig. 5(c). From the ozone mass streamfunction we infer that the circulation of ozone through the stratosphere provides a significant contribution to the dayside-to-nightside transport. The downward ozone transport at the ϕ' of the Rossby gyres ($-60 < \phi' < 0°$) indicates that this stratospheric dayside-to-nightside circulation drives ozone-rich air into the Rossby gyres and thus leads to ozone maxima on the nightside.

Fig. 6 again shows Ψ'_{m,O_3}, now separated into four ranges of λ'. Each of these λ'-ranges corresponds to a distinct feature of the ozone distribution in Fig. 3(a). Fig. 6(a) shows the λ'-range that contains the low-λ' gyre ($\lambda' > 320°$ and $\lambda' \leq 70°$), and we can identify the dayside-to-nightside transport of ozone-rich air, followed by descending motion at ϕ' corresponding to the location of the Rossby gyres. The ozone is supplied from part of its production region (see Fig. 4) between pressures of 0.2 and 20 hPa. Fig. 6(b) shows the low-λ'-range that does not contain the gyres and instead includes the nightside-to-dayside component of the equatorial jet. Ψ'_{m,O_3} shows that there is a stratospheric clockwise circulation, but that this is separated from the lower parts of the atmosphere by an anticlockwise circulation at the ϕ' corresponding to the Rossby gyres and misses part of the ozone production regions between 10 and 100 hPa. Therefore, for $70 < \lambda' \leq 110°$, no ozone accumulation is found following the stratospheric overturning circulation. Fig. 6(c) again indicates dayside-to-nightside transport of ozone-rich air, with ozone for the mid-λ' gyre ($110 < \lambda' \leq 220°$) being supplied from the ozone production regions between pressures of 0.2 and 20 hPa. Lastly, Fig. 6(d) shows that in the final non-gyre range ($220 < \lambda' \leq 320°$) there is a stratospheric overturning circulation transporting ozone-rich air, but this circulation misses part of the ozone production region between 0.3 and 10 hPa and is generally weaker than for the ranges containing the gyres. Furthermore, the air that descends below ∼10 hPa will meet the equatorial jet, leading to chemical destruction of ozone (due to HO_x-rich air from the dayside) or advection back to the dayside followed by photochemical destruction. Therefore, this λ'-range is not accumulating ozone in the lower part of the atmosphere.

Our interpretation of the atmospheric dynamics is supported by an age-of-air tracer experiment. In Fig. 7, we show the zonally averaged time evolution of the age-of-air tracer during the model spin-up period. As a passive tracer, it is only affected by dynamical processes in the UM, including both advection and convection. The age-of-air tracer is initialized at 0 s and provides a measure of the amount of time that has passed since an air parcel was last found in the lowest layers of the atmosphere (below ∼2 km or 700 hPa). As such, the tracer measures the time it takes a parcel to rise from these lowest layers into the stratosphere. The tracer values are reset to 0 in the lowest layers at every model time-step. With the evolution of the age-of-air tracer over ϕ' in Fig. 7 we show that air rises over and around the substellar point, already providing much younger air to the dayside troposphere (<15 km) after 10 d of simulation. After 100 d, we find that most of the troposphere has been replenished with much younger air, except for the nightside gyres between $-60° < \phi' < 0°$. This picture persists after 500 d, showing that the age-of-air tracer in the nightside gyres is fed by older air from the stratosphere. From this experiment, we can conclude that the mechanism affects any long-lived tracer, and thus might also be important for the distribution of photochemical hazes (Steinrueck et al. 2021).

We conduct a similar experiment for the ozone tracer, after its constant initialization at MMRs of 10^{-9}. Fig. 8 shows the time evolution of the ozone number density, which can be directly compared to Fig. 3(b). At the start of the simulation ($t = 1$ d), ozone is produced on the dayside hemisphere. After 10 d, the peak in ozone number density has moved to higher altitudes, entering the stratosphere (above ∼100 hPa). After 100 d of simulation, we can clearly see the planetary ozone layer forming in the stratosphere. The peak has moved up again since the passage of radiation through the atmosphere becomes shorter with more ozone. In the troposphere, we can see the accumulation of ozone in the nightside gyres. These abundances are similar to those in the lower stratosphere, and the contour levels bend downwards at the gyre locations. This same distribution persists after 500 d, and way beyond the spin-up period as shown in Fig. 3(b). This confirms that after ozone forms on the

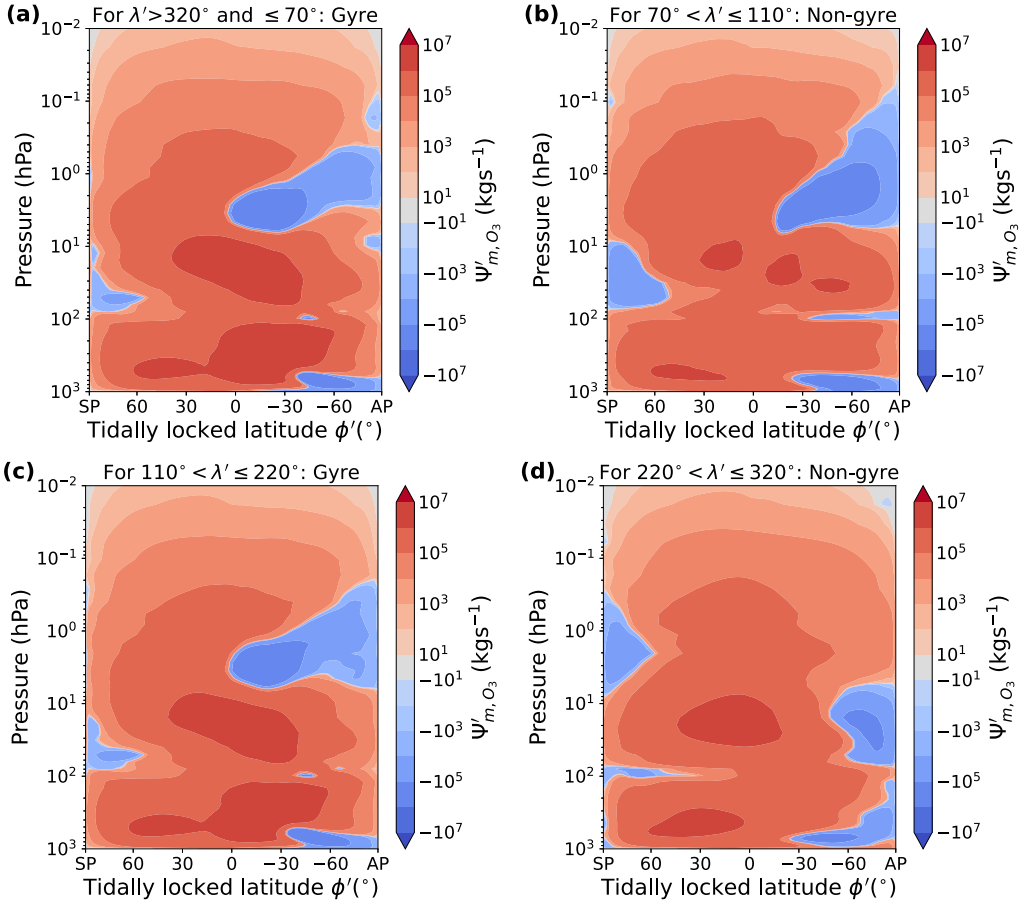

Figure 6. The zonal mean meridional ozone mass streamfunction Ψ'_{m,O_3} (equation 4) in tidally locked coordinates, for ranges of tidally locked longitude λ' as shown by the titles of each of the four panels. Panels (a) and (c) denote λ'-ranges corresponding to the locations of the ozone accumulation in the Rossby gyres, following the distribution of ozone in Fig. 3. The λ'-ranges in panels (b) and (d) correspond to the regions containing the superrotating jet. As such, panels (a) and (c) map out the meridional extent of the transport of ozone-rich air to the nightside.

dayside, the stratospheric circulation drives ozone to the nightside and into the gyres.

To further diagnose the nightside descent of ozone molecules into the gyres, we can define the vertical flux of ozone across pressure or altitude levels as

$$F_{O_3} = \int_{P_{max}}^{P_{min}} (w \cdot n_{O_3}) \mathrm{d}P, \tag{9}$$

where w is the vertical wind velocity (m s^{-1}) and n_{O_3} the ozone number density in molecules m^{-3}. Negative values correspond to downward transport and positive values to upward transport of ozone. The integration between pressure levels P_{max} and P_{min} is done to determine the total flux exchange between the stratosphere and troposphere. Using the streamfunctions in Fig. 5 and the ozone distribution in Fig. 3(b), we determine that downward transport between ∼200 and 8 hPa drives the ozone accumulation. Fig. 9 shows the vertical flux of ozone, integrated over pressures between 190 and 8 hPa. Generally, we find a relatively small but hemisphere-wide upward flux on the dayside. The nightside gyre locations stand out with a relatively strong downward flux. Hence, the ozone that was produced in the stratosphere will be transported downward into the troposphere at the gyre locations. Combining the streamfunctions, the tracer evolution experiments and the vertical ozone flux, we find that the stratospheric overturning circulation provides a connection between the ozone production regions and the nightside gyres, leading to the accumulation of ozone in the latter. To the authors' knowledge, this is the first time this connection has been reported.

3.3 Dynamical and chemical time-scales

As outlined in Section 2.2, we extract the three wind components and reaction fluxes for the Chapman termination reaction (R1) and rate-limiting step of the dominant HO_x catalytic cycle (R2) to calculate dynamical (τ_u, τ_v, and τ_w) and chemical lifetimes (τ_{Chap} and τ_{HO_x}) around the planet. Fig. 10 shows the different lifetimes at each of the four locations. From Fig. 10(a), we conclude that the dynamical lifetimes are shorter than the chemical lifetimes at all four locations, indicating that dynamics can be an important driver of disequilibrium abundances in this pressure range.

In Fig. 10(b), we highlight the differences between τ_u and τ_w, for the troposphere (<100 hPa) and lower stratosphere (between 100 and 10 hPa), by using the fraction τ_u/τ_w. Vertical transport is the dominant process for $\tau_u/\tau_w > 1$ (right of the vertical line) and horizontal transport for $\tau_u/\tau_w < 1$ (left of the vertical line). Around the substellar point (solid lines), we determine that vertical mixing dominates the troposphere ($\tau_u/\tau_w > 1$) and that zonal mixing (τ_u) starts to take over for $P > 80$ hPa. Above this pressure, chemical abundances at the substellar point can be spread out zonally

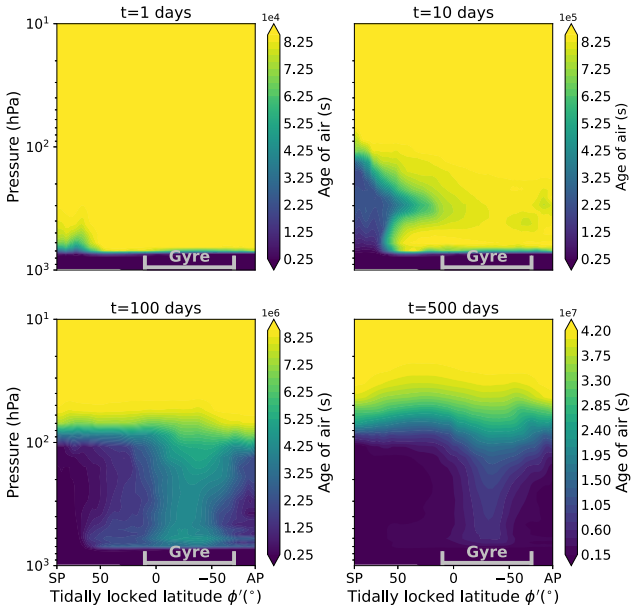

Figure 7. Age-of-air tracer during the spin-up of the simulation, showing the mean meridional distribution in tidally locked coordinates. As a passive tracer, it is only affected by dynamical processes (advective and convective). As such, the age-of-air measures the time it takes a parcel to rise from the lowest atmospheric layers (at ∼2 km or 700 hPa) into the stratosphere. The tracer values are reset to 0 in the lowest atmospheric layers at every model time-step. We also show the tidally locked latitudes corresponding to the nightside gyres in grey.

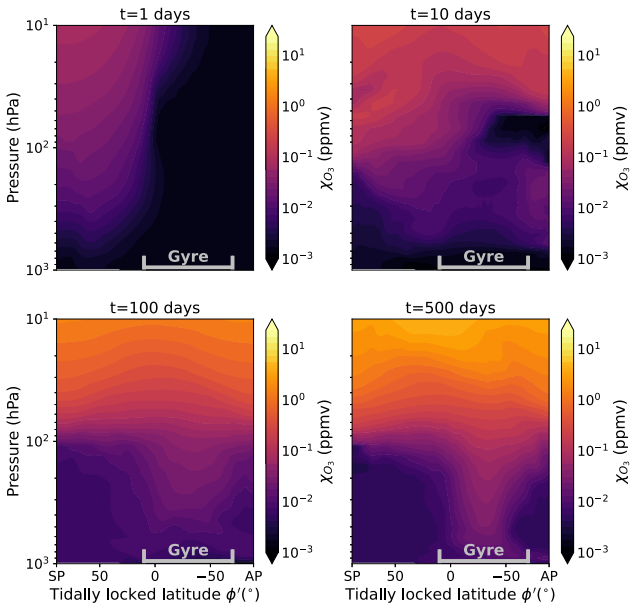

Figure 8. Ozone mole fraction during the spin-up of the simulation, showing the mean meridional distribution in tidally locked coordinates. Similar to Fig. 7, but now for a chemically active species. We also show the tidally locked latitudes corresponding to the nightside gyres in grey.

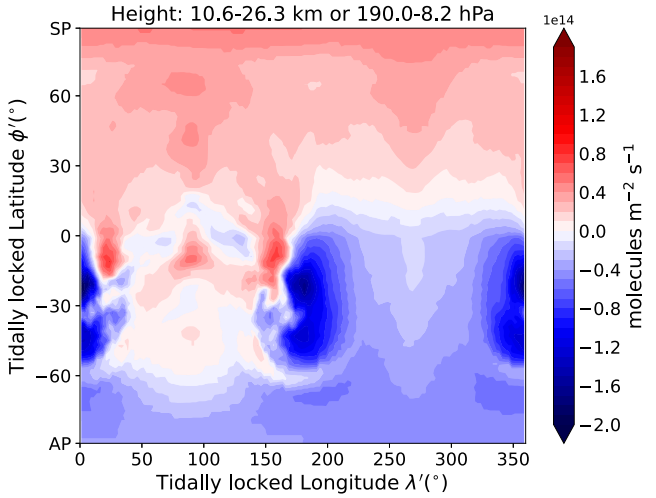

Figure 9. Vertical flux of ozone (F_{O_3} in molecules m^{-2} s^{-1}) between $P_{max} = 190$ hPa and $P_{min} = 8.2$ hPa. The predominantly downward exchange at the locations of the Rossby gyres illustrates how the enhanced ozone column densities are driven by the downward motions that are part of the stratospheric dayside-to-nightside circulation.

towards the nightside, connecting with the ozone-producing region that is part of the overturning circulation from Section 3.2. At the nightside location of the jet, $\tau_u/\tau_w < 1$, and the zonal wind is capable of homogenizing any vertically driven disequilibrium. The circumnavigating jet then leads to the relatively thin ozone column for $70^\circ < \lambda' < 110^\circ$ and $220^\circ < \lambda' < 320^\circ$ in Fig. 3 (across all ϕ'). At the locations of the nightside gyres, Fig. 10(b) shows that τ_u and τ_w are intermittently the smallest, indicating that both vertical and zonal mixing can drive disequilibrium abundances. However, as mentioned in Section 3.2, the edges of the gyres act as mixing barriers. Hence, the zonal transport leads to homogenization within the gyres. Vertical mixing that is part of the overturning dayside-to-nightside circulation is dominant between ∼200 and 50 hPa at the gyre locations. This vertical mixing drives the observed disequilibrium abundances of tropospheric ozone at the gyre locations, and thus the maximum ozone column densities in Fig. 3(a).

3.4 Lightning-induced chemistry

The impact of the overturning circulation goes beyond the spatial distribution of ozone, as is evident from the distribution of the age-of-air tracer as shown in Fig. 7. Any tracer, gaseous or non-gaseous phase, can continue to circulate as long as its chemical lifetime exceeds the dynamical time-scales. Hence, the overturning circulation is relevant for any so-called long-lived atmospheric tracer. We performed similar analyses using the species-weighted streamfunction as defined in Section 2.2 on the distributions of nitric acid (HNO_3) and dinitrogen pentoxide (N_2O_5). Both of these species are signatures of lightning-induced chemistry in our simulations (Braam et al. 2022). They are non-radical species with relatively long chemical lifetimes and are mainly destroyed by photolysis and wet deposition (rainout). In the dayside troposphere, the lifetimes against wet deposition are $\sim 10^{-2}$–10^2 yr, while higher up in the atmosphere the lifetimes against photolysis are $\sim 10-10^2$ yr. On the nightside, these loss processes are absent and thus their chemical lifetimes approach infinity.

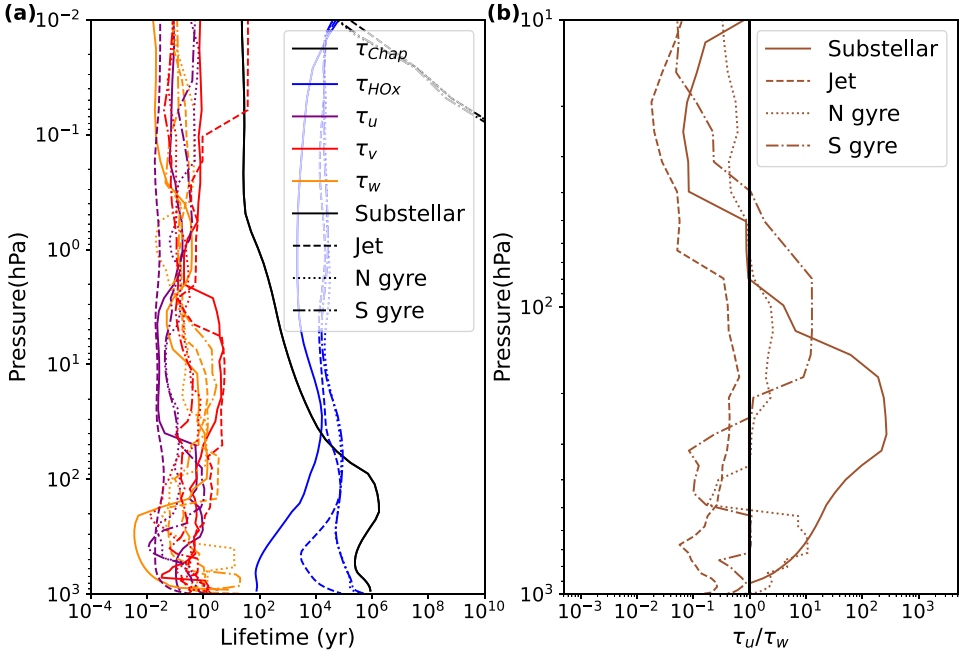

Figure 10. Dynamical and chemical lifetimes over four locations in the atmosphere: the substellar point, two regions over the gyres and one region over the nightside jet. (a) τ_u, τ_v, and τ_w denote the dynamical lifetime versus zonal, meridional, and vertical transport, respectively. τ_{Chap} and τ_{HO_x} show the chemical lifetimes of ozone versus loss by the Chapman termination reaction (R1) and the dominant HO_x catalytic cycle (R2), respectively. From the comparatively long chemical lifetimes, we can deduce that dynamical processes control the chemical abundances. (b) The fraction of the zonal to vertical dynamical lifetimes in the lower stratosphere (between 100 and 10 hPa) and troposphere (<100 hPa), along with a vertical line indicating where they are equal ($\tau_u/\tau_w = 1$). Vertical transport is the dominant process for $\tau_u/\tau_w > 1$ and horizontal transport for $\tau_u/\tau_w < 1$.

Table 2. Species-weighted streamfunctions $\Psi'_{\text{m},x}$ in kg s^{-1} averaged over pressure levels corresponding to the troposphere and stratosphere. Shown for ozone and lightning-induced chemistry in the form of HNO_3 and N_2O_5.

	$\Psi'_{\text{m,O}_3}$	$\Psi'_{\text{m,HNO}_3}$	$\Psi'_{\text{m,N}_2\text{O}_5}$
Troposphere	9.70×10^5	9.47×10^{-1}	4.44×10^{-2}
Lower stratosphere	6.09×10^5	6.07×10^{-3}	1.50×10^{-3}

We calculate $\Psi'_{\text{m,HNO}_3}$ and $\Psi'_{\text{m,N}_2\text{O}_5}$ similar to equation (4), and calculate the mean of each of the species-weighted streamfunctions over the troposphere ($>10^2$ hPa) and mid-to-lower stratosphere ($1 < P < 10^2$ hPa). The results are shown in Table 2.

The circulation cells weighted by HNO_3 and N_2O_5 are strongest in the troposphere, at ∼0.95 and ∼0.04 kg s^{-1}, respectively, because of the strong overturning circulation here (see Fig. 5b). The troposphere is also the region where lightning flashes are predicted to occur and thus where HNO_3, N_2O_5, and their precursors are produced (Braam et al. 2022). The factor 10^6 and 10^7 difference with the ozone-weighted streamfunction in Table 2 is a consequence of the much lower predicted abundances of HNO_3 and N_2O_5. Moving up to the stratosphere, we find that the ozone-weighted streamfunction is similar to the streamfunction in the troposphere, providing the connection to the nightside gyres. For HNO_3 and N_2O_5, the streamfunction is ∼30 and 150 times lower in the stratosphere, due to low levels of stratospheric HNO_3 and N_2O_5 with the absence of lightning-induced chemistry at those pressure levels. Because of the lack of stratospheric HNO_3 and N_2O_5, the overturning circulation will not be able to accumulate these species at the locations of the nightside gyres (as is evident in the spatial distribution in fig. 10 of Braam et al. 2022).

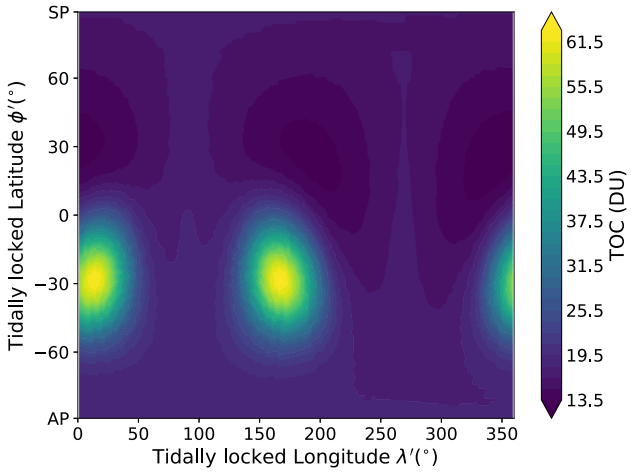

Figure 11. Total ozone column density, over 50 orbits of Proxima Centauri b for the 0.01 PAL O_2 case. Again we see a spatially variable ozone layer with accumulation at the locations of the nightside Rossby gyres ($-60 < \phi' < 0$).

3.5 0.01 PAL O_2 simulations

Fig. 11 shows the ozone column density for a synchronously rotating planet around Proxima Centauri, assuming the atmosphere has 0.01 PAL O_2. We find lower ozone column densities (global average of 20 DU) with decreased O_2 levels, agreeing with a reduced ozone column for Earth around the Sun for decreased O_2 levels (Cooke et al. 2022). Nevertheless, we still see significant spatial variability and the accumulation of ozone in the nightside gyres, similar to the 1 PAL case in Fig. 3(a). The highest ozone column densities of 63

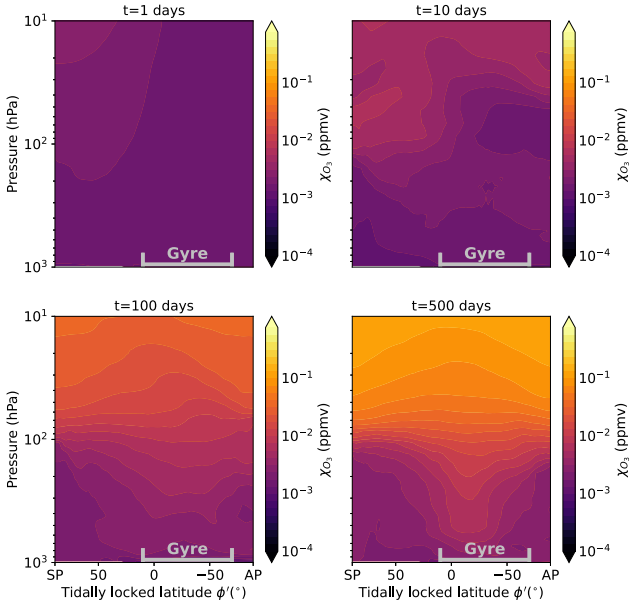

Figure 12. Ozone mole fraction during the spin-up of the simulation for the 0.01 PAL O_2 case, showing the mean meridional distribution in tidally locked coordinates. We also show the tidally locked latitudes corresponding to the nightside gyres in grey, and can see that the accumulation of ozone here happens in a similar way as in Fig. 8.

DU are found at the gyre locations (as compared to 1401 DU in the 1 PAL case). The similarity in the spatial variability to the 1 PAL O_2 atmosphere suggests the existence of a similar circulation-driven mechanism.

To explore the capability of a 0.01 PAL O_2 atmosphere to support a stratospheric dayside-to-nightside circulation, Fig. 12 shows the time evolution of the ozone mole fraction during part of the spin-up of this simulation. From day 1, we see that ozone starts to form above 100 hPa, and starts to circulate towards the nightside after 10 d. After 100 d, the ozone layer is present between 40 and 3 hPa, and we see downward movement from the ozone layer at the gyre locations ($-60^\circ < \phi' < 0^\circ$). These features are even more pronounced on day 500, and persists afterwards. The vertical distribution and its temporal evolution show that a similar stratospheric dayside-to-nightside circulation followed by subsidence at the gyre locations drives the ozone accumulation over the gyres. Further diagnosis of the mechanism using the streamfunctions and vertical ozone flux (not shown) confirm this picture.

4 DISCUSSION

In this section, we start by describing the driving mechanism for the overturning circulation. We then show its impact on other long-lived tracers and discuss relevant temporal variability in the atmospheres of synchronously rotating exoplanets. Lastly, we produce synthetic emission spectra to investigate the observational impact of circulation-driven ozone chemistry.

4.1 Driving mechanism of the overturning circulation

The tropospheric overturning circulation for moist, rocky exoplanets in a synchronous orbit is driven by the absorption of incoming stellar radiation and latent heat release on the dayside, and longwave (LW) radiative cooling on the nightside (e.g. Showman et al. 2013; Boutle et al. 2017). Wang & Yang (2022) study dry, rocky planets rotating synchronously around an M-dwarf star and find that the overturning circulation is indirectly driven by the stellar radiation, in the form of nightside cooling by CO_2. They find that an overturning circulation forms in a N_2–CO_2 atmosphere, but not in a pure N_2 atmosphere (Wang & Yang 2022). Prescribed CO_2 distributions from Wang & Yang (2022) show that shortwave (SW) absorption on the planetary dayside only has a limited impact on the overturning circulation. CO_2 can cool an atmosphere when it is found in layers exhibiting a temperature inversion (Wang & Yang 2022). Enhanced infrared emission from increasing CO_2 levels cools the Earth's stratosphere (Luther, Wuebbles & Chang 1977; Brasseur & Hitchman 1988; Langematz et al. 2003; Shine et al. 2003; Fomichev et al. 2007). On synchronously rotating planets, this can induce a downward motion on the nightside that subsequently drives dayside-to-nightside overturning circulation.

Since we focus on the stratosphere, which is relatively dry even for a moist climate of a rocky exoplanet in a synchronous orbit, we can build upon these results in identifying the driving mechanism. The SW atmospheric heating rates in Fig. 13(a) show that CO_2 (the green line) acts as an important SW absorber on the dayside. The main absorber in the troposphere is H_2O, whereas CO_2 starts to become dominant above ∼170 hPa. In line with Wang & Yang (2022), we find that heating due to SW absorption by CO_2 plays a minor role in the troposphere. However, in the stratosphere CO_2 absorption can become important because peak emissions from M-dwarfs are emitted at near-infrared (NIR) wavelengths, relatively long as compared to other stars. CO_2 (and H_2O) have strong NIR absorption bands (Selsis et al. 2007; Turbet et al. 2016; Lobo et al. 2023), which explains why CO_2 is the dominant absorbing species above ∼170 hPa, in contrast to ozone in the Earth's stratosphere. As expected, the total dayside heating rates (solid black line) greatly exceed the nightside values (dashed line), forming a direct driver for the overturning circulation. Additionally, Fig. 13(b) shows the LW heating rates, with negative values indicating cooling of the atmosphere. The black lines show stronger LW cooling on the nightside as compared to the dayside. Again, CO_2 is mainly responsible for these cooling rates, due to its presence in temperature inversion layers at ∼100 and ∼1 hPa. This radiative cooling on the nightside drives a large-scale downwelling which, together with SW heating on the dayside, supports the stratospheric overturning circulation (Edson et al. 2011; Koll & Abbot 2016; Wang & Yang 2022), and can explain the ozone maxima at the locations of the nightside gyres. The atmospheric pressure within the gyre is relatively low, analogous to the eye of tropical cyclones (Schubert et al. 2007). Such a pressure gradient naturally induces downward transport at the gyre locations. An important follow-up to this study is to investigate the ozone distribution for a variety of rotation states (see e.g. Carone et al. 2018; Haqq-Misra et al. 2018; Chen et al. 2019) in light of the circulation-driven chemistry proposed here.

4.2 Long-lived atmospheric tracers

The stratospheric dayside-to-nightside circulation affects other tracers than ozone, as we show with the results for the age-of-air in Section 3.2 and the lightning-induced species in Section 3.4. In the presence of stellar flares, Ridgway et al. (2023) show that the gyres are depleted in ozone (see their fig. 12). This can also be explained by the stratospheric overturning circulation, since flare-induced chemistry will result in a large amount of nitric oxide (NO) and nitrogen dioxide (NO_2) (together known as the NO_x chemical

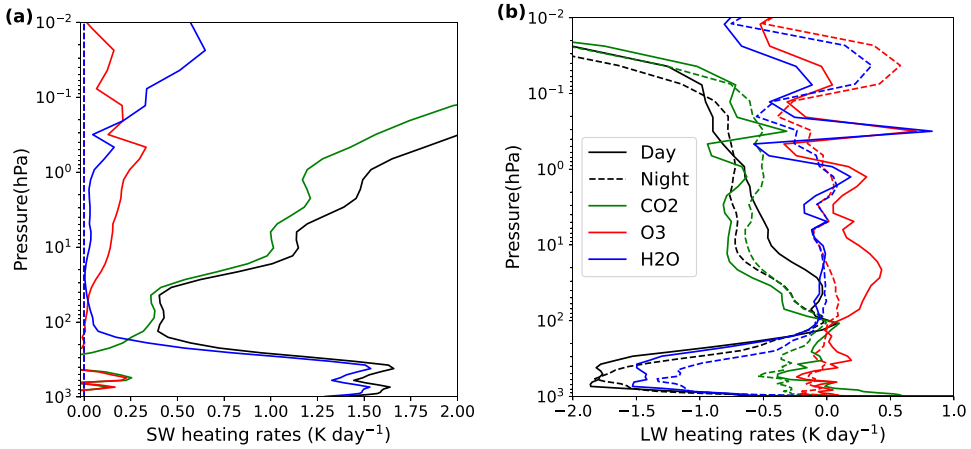

Figure 13. Atmospheric heating (and cooling) rates, for (a) the SW radiation and (b) LW radiation. Solid lines show the hemispheric average over the dayside and dashed lines over the nightside. The coloured lines indicate the individual components contributing to the total heating rates in black, showing that CO_2 (green) becomes the dominant contributor to the dayside SW heating rates and that LW cooling is also mainly driven by CO_2.

family) at stratospheric levels (Ridgway et al. 2023). This NO_x can follow the stratospheric overturning circulation from the dayside to the nightside. Once on the nightside, it can be transported downward at the location of the gyres and locally deplete the ozone through the NO_x catalytic cycle (Ridgway et al. 2023), given that flares produce sufficient NO_x.

The impact of the overturning circulation on the distribution of ozone has analogies with studies that simulate tracers in the atmospheres of synchronously rotating hot Jupiters. Parmentier et al. (2013) identified dynamical mixing in hot Jupiter atmospheres as a process leading to cold trapping of condensible species on the planetary nightside. Their experiments involve gravitational settling as a source of these condensed particles, which leads to a gradient of tracer abundance, with fewer particles as we move up through the atmosphere. Upward mixing induced by the large-scale dynamics balances the settling of these particles, preventing the complete depletion of particles and inducing a strong spatial variation in the tracer abundances. The extent of the mechanism depends on the strength of frictional drag (Komacek, Showman & Parmentier 2019). The mechanism does not require convection but follows the large-scale atmospheric motions that are ultimately driven by the dayside–nightside heating contrast (Parmentier et al. 2013), as is the case for the circulation-driven ozone distribution discussed here. Another example of a long-lived tracer is photochemical haze, which is also expected to form at stratospheric altitudes (e.g. Arney et al. 2017) and, for synchronously rotating exoplanets, only on the dayside of a planet (e.g. Steinrueck et al. 2021). Steinrueck et al. (2021) show that the 3D distribution of small photochemical hazes ($\leq$10 nm) in hot Jupiter atmospheres is also driven by dynamical mixing. The highest tracer abundances are found above the production peak, indicating upwelling on the dayside. Then a divergent flow leads to transport towards the poles and the nightside. On the nightside, the haze particles are then advected downward and get trapped in the mid-latitude gyres (Steinrueck et al. 2021). These dynamically induced asymmetries can produce distinctions between a planet's terminator regions, as shown for hot Jupiters (Drummond et al. 2020; Steinrueck et al. 2021; Zamyatina et al. 2023). Following up on the results presented here, we will investigate the potential terminator variability of the circulation-driven ozone distribution and its observability.

4.3 Time variability

Besides spatial variability in tracer distributions, simulations of synchronously rotating exoplanets exhibit several modes of temporal variability. The formation of the Rossby gyres is due to the thermal forcing asymmetries (Showman & Polvani 2010, 2011). Cohen et al. (2023) show that these gyres oscillate over longitude λ, with the extent depending on the planet's rotation period and thus dynamical state. Planets with a slower rotation rate have longer oscillation periods, resulting in a 157.5-d oscillation for Proxima Centauri b, which was determined from the temporal evolution of the cloud cover (Cohen et al. 2023). Using a dynamical systems approach, Hochman, Luca & Komacek (2022) compare TRAPPIST-1e in a synchronous orbit to Earth and find that the climate extremes on a synchronously rotating exoplanet are more sensitive to changes in the partial pressure of CO_2.

Since the stellar spectra are constant in time and the planet rotates in a 1:1 resonant orbit without eccentricity and/or obliquity, such variability has to be produced by internal atmospheric variability. Cohen et al. (2023) show that feedback between cloud cover and the incoming stellar radiation can influence the dynamics and drive zonal movement of the gyres, leading to variations in humidity and cloud cover over time. The accumulation of ozone (Fig. 3) depends on the gyres so we expect there also to be a corresponding variation in atmospheric ozone. To verify this, in Fig. 14 we track the temporal evolution of the tidally locked coordinates corresponding to the maximum in the ozone layer and the minimum in the vertical flux of ozone (F_{O_3}, thus corresponding to the strongest downward flux). Fig. 14(a) shows ϕ' and Fig. 14(b) λ' corresponding to these extrema, and the approximate extents of the gyres are indicated in yellow. The locations of the maximum ozone column density and minimum vertical flux are not perfectly aligned, because the maximum ozone column density corresponds to a long-term mean location of the gyre and thus depends on vertical fluxes over an extended period. The minimum vertical flux represents a snapshot in time and is also impacted by the upward flux from the gyre (see the red regions in Fig. 9). From Fig. 14(a), we determine that the maximum ozone column density is generally found at ϕ' corresponding to the gyre locations, with a small meridional variation over time. The minimum F_{O_3} shows more variability in tidally locked latitude, but the strongest downward flux is generally also located at the gyre locations. In Fig.

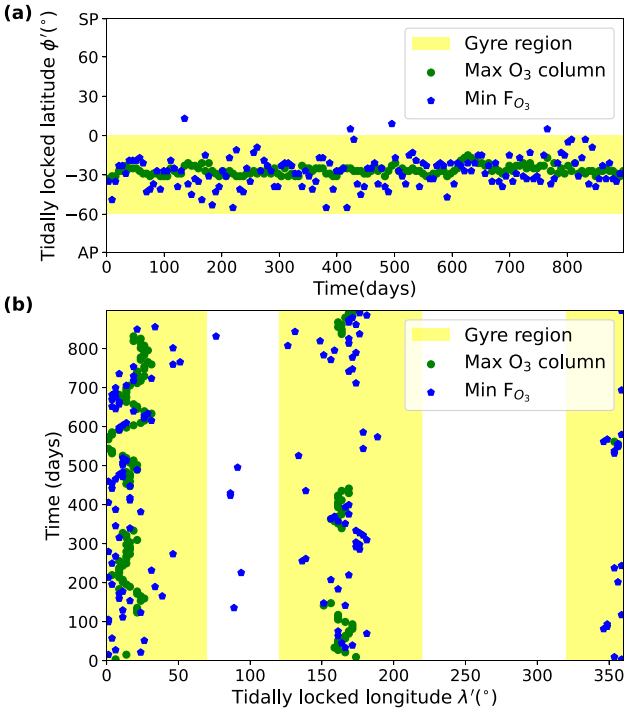

Figure 14. Temporal evolution of the locations of extremes in the ozone column density (see Fig. 3) and vertical ozone flux F_{O_3} as defined in equation (9). We extract the tidally locked latitude ϕ' and longitude λ' corresponding to the maximum ozone column density (shown as the green dots) and the minimum F_{O_3} (or the strongest downward flux, shown as the blue hexagons), to look for correlations between the two. Panels (a) and (b) show the temporal evolution of ϕ' and λ', respectively, and the yellow rectangles indicate the gyre locations.

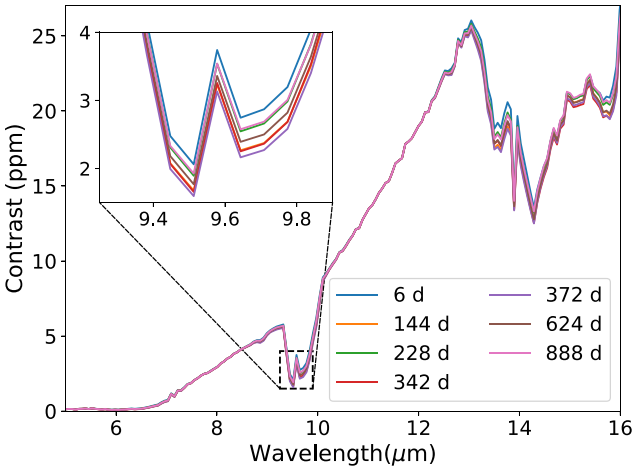

Figure 15. Simulated emission spectra of Proxima Centauri b, for a range of 6-d intervals informed by extrema in the gyre locations (Fig. 14). The legend shows the maximum day corresponding to each of the 6-d intervals. The inset region shows the region corresponding to the 9.6 μm ozone feature in greater detail.

14(b), we see the variations in the tidally locked longitude λ' over time. The low-λ' gyre typically hosts the maximum ozone column, but there are periods when the mid-λ' gyre hosts the maximum ozone column. The variations in the minimum F_{O_3} broadly align with the maximum in the ozone column density, following the gyre position that has the maximum ozone column at that time. The location of minimum F_{O_3} shows more variability due to its instantaneous nature.

We translate the temporal variability into simulated observables using the Planetary Spectrum Generator (PSG; Villanueva et al. 2018, 2022). To simulate an emission spectrum that includes half the planetary dayside and half the nightside, we extract the atmospheric pressure and temperature and mole fractions of relevant chemical species (N_2, O_2, CO_2, H_2O, O_3, N_2O, HNO_3, and N_2O_5) for these locations, take the zonal and meridional averages and compute radiative transfer with PSG. In Fig. 15, we show the resulting planet-to-star contrast for the *JWST*-MIRI wavelength range, along with a zoom-in that focuses on the ozone 9.6 μm feature. Using extrema in the gyre positions over time from Fig. 14, we simulate the emission spectra of Proxima Centauri b for different 6-d intervals and indicate the maximum day in the legend of Fig. 15. We find variations around the ozone features at 9.6 μm and between 14 and 16 μm (due to absorption by CO_2, H_2O, and ozone). Hence, the region around 9.6 μm is the place to look for ozone variability. Focusing on the region around 9.6 μm shows that the maximum temporal variations are about 0.5 ppm. Spectroscopic characterization of these absorption features to the level needed to identify these temporal variations is challenging, as detecting the features themselves would already require many days of co-added observations (Kreidberg & Loeb 2016). However, the recent photometric observations of the thermal emission from TRAPPIST-1 b with *JWST* indicate the telescope's capacity to observe favourable terrestrial exoplanets (Greene et al. 2023). Mission concepts such as the Large Interferometer For Exoplanets (Quanz et al. 2022) further utilize the mid-infrared in the characterization of terrestrial exoplanets and will have to consider the impact of 3D spatial and temporal variability in atmospheric dynamics and chemistry.

The hot Jupiter simulations of passive tracers by Parmentier et al. (2013) also exhibit significant temporal variability. Oscillations in the equatorial jet and variations in the dayside-to-nightside flow produce large local variations, which could again impact the spectroscopic observations of the planets, both when conducting extended observations and when observing the same object at two different points in time.

Another mode of variability in the atmospheres of exoplanets in synchronous orbits around M-dwarfs is the Longitudinally Asymmetric Stratospheric wind Oscillation (LASO; Cohen et al. 2022). Since this entails a stratospheric turnover of wind directions, it could be relevant for stratospheric ozone. Analysing ozone mole fractions over time, we find variations in the ozone mole fractions above ∼30 km (or ∼3.5 hPa) as a consequence of the LASO. However, these variations occur higher up in the atmosphere than the overturning circulation feeding the gyres and thus do not affect the gyre abundances significantly. Hochman et al. (2022) investigate atmospheric dynamics, atmospheric variability and climate extremes using a dynamical systems approach. As compared to an Earth analogue, they find significantly different spatial variability in the climate extremes for TRAPPIST-1 e, assuming it is synchronously rotating. Varying basic parameters like the partial pressure of CO_2, Hochman et al. (2022) find that the climate and climate extremes on TRAPPIST-1e are more sensitive than the Earth analogue. Importantly, climate variability on synchronously rotating exoplanets may be of a similar level as the variability produced by the seasons on Earth (Hochman et al. 2022), which seems to be supported by our findings on variability in the ozone column densities. We see variations in ozone column densities of up to ±8 DU on the dayside and as much as ±30 DU close to the gyres on the nightside, corresponding to their

zonal movement as shown in Fig. 14. Tropospheric ozone over the Earth's northern mid-latitudes shows a seasonal variability of 7–8 DU, related to stratosphere–troposphere exchange (Hsu & Prather 2009). A comprehensive comparison is beyond the scope of this paper, but we plan to explore this further as part of an in-depth investigation of the observability of the circulation-driven ozone distribution.

External drivers of variability in exoplanet atmospheres can also drive temporal variations in spectral features. Stellar flares are a likely cause for planets orbiting M-dwarf stars, and can modulate the abundance of photochemically produced species such as ozone, HO_x, and NO_x (Segura et al. 2010; Scheucher et al. 2018; Chen et al. 2021; Ridgway et al. 2023). Orbital configuration, in particular the eccentricity, can cause variations in the abundance of chemical species over time, as Liu et al. (2023) showed for the water vapour abundance on an Earth-like planet. We leave an expansion of circulation-driven atmospheric chemistry in eccentric orbits for future work. In compact multiplanet systems, planet–planet interactions may produce spin-orbit variations that cause libration of the substellar point (Chen et al. 2023). This libration strongly affects the climate of planets orbiting close to the outer edge of the Habitable Zone and may bring temporal variations in photo- and thermochemistry along. Lastly, impacts of planetesimals can cause loss of atmospheric mass (Schlichting & Mukhopadhyay 2018) and thereby affect the extent of spectral features. Identifying the effects of each of these external drivers will benefit from understanding internal drivers of atmospheric variability, and vice versa.

5 CONCLUSIONS

We use a 3D CCM (UM-UKCA) to study the spatial structure of the ozone layer on an exoplanet rotating in a 1:1 spin-orbit resonance around an M-dwarf star, using the parameters corresponding to Proxima Centauri b. Our results are relevant for similar M-dwarf orbiting planets, specifically for slowly rotating planets with a strong overturning circulation and a single equatorial jet in the troposphere. We investigate the spatial variability in the ozone layer and specifically the accumulation in two nightside ozone maxima, in the form of maximum ozone columns at the locations of the permanent Rossby gyres. Our work builds upon previous studies that have shown that M-dwarf radiation supports the emergence of a global ozone layer.

We show that stratospheric dayside-to-nightside circulation and downward motion over low-pressure nightside gyres can explain the spatial variability in ozone. The photochemistry required to initiate the Chapman mechanism of ozone formation is limited to the dayside hemisphere, given the absence of incoming stellar radiation on the nightside. We find a connection between the ozone production regions on the dayside and the nightside hemisphere, using the transformation to the tidally locked coordinate system. Meridional streamfunctions that we calculate from the divergent wind component illustrate the existence of a stratospheric dayside-to-nightside overturning circulation. This circulation consists of a single circulation cell characterized by upwelling motion in the ozone production regions, followed by stratospheric dayside-to-nightside transport and downwelling motions at the locations of the nightside gyres. The downwelling motion produces a flux of ozone from the stratosphere into the troposphere, leading to well-defined maxima in the ozone distribution. We find that the stratospheric dayside-to-nightside circulation controls the ozone distribution for both a 1 PAL O_2 and a 0.01 PAL O_2 atmosphere. The circulation-driven ozone chemistry impacts spectroscopic observations, although the impact of temporal variability is limited to sub-ppm levels in emission spectra.

By investigating the impact of the stratospheric overturning circulation on lightning-induced chemical species (also limited to dayside production, but solely in the troposphere), we can explain why these species do not show a similar accumulation in the nightside gyres. We show with an age-of-air tracer experiment that the stratospheric overturning circulation also affects other tracer species in the stratosphere, including gaseous chemical tracers and particulate components of photochemical haze, with the only requirement that the dynamical lifetimes are sufficiently short compared to chemical time-scales.

We identify hemispheric contrasts in atmospheric heating and cooling rates as the driver for the overturning circulation. Dayside heating can directly drive the overturning circulation, and nightside cooling provides an indirect component by inducing local downward motion. The relatively low atmospheric pressure over the nightside gyres further induces downward motion here. Since the stratosphere is relatively dry, CO_2 absorption is the main contributor to these heating and cooling rates. Ozone absorption also contributes to the rates, but its contribution is weaker than CO_2 since M-dwarf fluxes peak close to absorption bands of CO_2.

For the first time, we find a connection between the ozone-producing dayside of synchronously rotating planets and the simulated ozone maxima on the nightside, covering hemispheric scales and multiple vertical levels in the stratosphere and troposphere. The role of the stratospheric dayside-to-nightside circulation in driving the ozone distribution around the planet illustrates the necessity of 3D model to capture atmospheric processes correctly. Any robust interpretation of spectroscopic observations will need to understand the spatial and temporal variability of chemical species due to such circulation-driven chemistry.

ACKNOWLEDGEMENTS

We are very grateful to Denis Sergeev for his contribution to the coordinate transformations and valuable feedback on the manuscript. MB kindly thanks Ludmila Carone for discussing circulation regimes on synchronously rotating exoplanets. We are grateful to the anonymous reviewer whose comments helped to improve this paper.

MB, PIP, and LD are part of the CHAMELEON MC ITN EJD which received funding from the European Union's Horizon 2020 research and innovation programme under the Marie Sklodowska-Curie grant agreement no. 860470. PIP acknowledges funding from the STFC consolidator grant no. ST/V000594/1. LD acknowledges support from the KU Leuven IDN grant IDN/19/028 and from the FWO research grant G086217N. MC acknowledges the funding and support provided by the Edinburgh Earth, Ecology, and Environmental Doctoral Training Partnership and the Natural Environment Research Council (grant no. NE/S007407/1). NJM was supported by a UKRI Future Leaders Fellowship (grant no. MR/T040866/1), a Science and Technology Facilities Council consolidated grant (ST/R000395/1), and the Leverhulme Trust through a research project grant (RPG-2020-82).

We gratefully acknowledge the use of the MONSooN2 system, a collaborative facility supplied under the Joint Weather and Climate Research Programme, a strategic partnership between the Met Office and the Natural Environment Research Council. Our research was performed as part of the project space 'Using UKCA to investigate atmospheric composition on extra-solar planets (ExoChem)'. For the purpose of open access, the authors have applied a Creative

DATA AVAILABILITY

All the CCM data were generated using the Met Office Unified Model and UK Chemistry and Aerosol model (https://www.ukca.ac.uk/), which are available for use under licence; see http://www.metoffice.gov.uk/research/modelling-systems/unified-model. The data underlying this article will be shared on reasonable request to the corresponding author, mainly motivated by the size of the data.

We used the IRIS (Met Office 2022) and AEOLUS (Sergeev & Zamyatina 2022) PYTHON packages for the post-processing of model output. Scripts to process and visualize the data are available on github: https://github.com/marrickb/o3circ_code.

REFERENCES

Archibald A. T. et al., 2020, Geosci. Model Dev., 13, 1223
Arney G. N., Meadows V. S., Domagal-Goldman S. D., Deming D., Robinson T. D., Tovar G., Wolf E. T., Schwieterman E., 2017, ApJ, 836, 49
Barnes R., 2017, Celest. Mech. Dyn. Astron., 129, 509
Bian H., Prather M. J., 2002, J. Atmos. Chem., 41, 281
Boutle I. A., Mayne N. J., Drummond B., Manners J., Goyal J., Hugo Lambert F., Acreman D. M., Earnshaw P. D., 2017, A&A, 601, A120
Braam M., Palmer P. I., Decin L., Ridgway R. J., Zamyatina M., Mayne N. J., Sergeev D. E., Abraham N. L., 2022, MNRAS, 517, 2383
Brasseur G., Hitchman M. H., 1988, Science, 240, 634
Brown A. R., Beare R. J., Edwards J. M., Lock A. P., Keogh S. J., Milton S. F., Walters D. N., 2008, Bound. Layer Meteorol., 128, 117
Butchart N., 2014, Rev. Geophys., 52, 157
Carone L., Keppens R., Decin L., 2014, MNRAS, 445, 930
Carone L., Keppens R., Decin L., 2015, MNRAS, 453, 2412
Carone L., Keppens R., Decin L., Henning T., 2018, MNRAS, 473, 4672
Chapman S., 1930, London Edinburgh Dublin Phil. Mag. J. Sci., 10, 369
Chen H., Wolf E. T., Kopparapu R., Domagal-Goldman S., Horton D. E., 2018, ApJ, 868, L6
Chen H., Wolf E. T., Zhan Z., Horton D. E., 2019, ApJ, 886, 16
Chen H., Zhan Z., Youngblood A., Wolf E. T., Feinstein A. D., Horton D. E., 2021, Nat. Astron., 5, 298
Chen H., Li G., Paradise A., Kopparapu R. K., 2023, ApJ, 946, L32
Cohen M., Bollasina M. A., Palmer P. I., Sergeev D. E., Boutle I. A., Mayne N. J., Manners J., 2022, ApJ, 930, 152
Cohen M., Bollasina M. A., Sergeev D. E., Palmer P. I., Mayne N. J., 2023, Planet. Sci. J., 4, 68
Cooke G. J., Marsh D. R., Walsh C., Black B., Lamarque J.-F., 2022, R. Soc. Open Sci., 9, 211165
Cooke G. J., Marsh D. R., Walsh C., Rugheimer S., Villanueva G. L., 2023, MNRAS, 518, 206
Dressing C. D., Charbonneau D., 2015, ApJ, 807, 45
Drummond B., Mayne N. J., Baraffe I., Tremblin P., Manners J., Amundsen D. S., Goyal J., Acreman D., 2018a, A&A, 612, A105
Drummond B. et al., 2018b, ApJ, 855, L31
Drummond B. et al., 2020, A&A, 636, A68
Eager J. K. et al., 2020, A&A, 639, A99
Edson A., Lee S., Bannon P., Kasting J. F., Pollard D., 2011, Icarus, 212, 1
Edwards J. M., Slingo A., 1996, Q. J. R. Meteorolog. Soc., 122, 689
Eyring V. et al., 2013, J. Geophys. Res. Atmos., 118, 5029
Fauchez T. J. et al., 2021, Planet. Sci. J., 2, 106
Fauchez T. J. et al., 2022, Planet. Sci. J., 3, 213
Fomichev V. I., Jonsson A. I., Grandpré J. d., Beagley S. R., McLandress C., Semeniuk K., Shepherd T. G., 2007, J. Clim., 20, 1121
France K. et al., 2016, ApJ, 820, 89
Geisler J. E., 1981, J. Atmos. Sci., 38, 1390
Gill A. E., 1980, Q. J. R. Meteorolog. Soc., 106, 447
Greene T. P., Bell T. J., Ducrot E., Dyrek A., Lagage P.-O., Fortney J. J., 2023, Nature, 618, 39
Gregory D., Rowntree P. R., 1990, Mon. Weather Rev., 118, 1483
Hammond M., Lewis N. T., 2021, Proc. Natl. Acad. Sci., 118, e2022705118
Haqq-Misra J., Kopparapu R. K., 2015, MNRAS, 446, 428
Haqq-Misra J., Wolf E. T., Joshi M., Zhang X., Kopparapu R. K., 2018, ApJ, 852, 67
Heng K., Frierson D. M. W., Phillipps P. J., 2011, MNRAS, 418, 2669
Hochman A., Luca P. D., Komacek T. D., 2022, ApJ, 938, 114
Hsu J., Prather M. J., 2009, J. Geophys. Res. Atmos., 114
Joshi M. M., Haberle R. M., Reynolds R. T., 1997, Icarus, 129, 450
Kasting J. F., Whitmire D. P., Reynolds R. T., 1993, Icarus, 101, 108
Koll D. D. B., Abbot D. S., 2015, ApJ, 802, 21
Koll D. D. B., Abbot D. S., 2016, ApJ, 825, 99
Komacek T. D., Abbot D. S., 2019, ApJ, 871, 245
Komacek T. D., Showman A. P., Parmentier V., 2019, ApJ, 881, 152
Kreidberg L., Loeb A., 2016, ApJ, 832, L12
Langematz U., Kunze M., Krüger K., Labitzke K., Roff G. L., 2003, J. Geophys. Res. Atmos., 108, 9
Lewis N. T., Lambert F. H., Boutle I. A., Mayne N. J., Manners J., Acreman D. M., 2018, ApJ, 854, 171
Liu B., Marsh D., Walsh C., Cooke G., 2023, MNRAS, 524, 1491
Lobo A. H., Shields A. L., Palubski I. Z., Wolf E., 2023, ApJ, 945, 161
Lock A. P., Brown A. R., Bush M. R., Martin G. M., Smith R. N. B., 2000, Mon. Weather Rev., 128, 3187
Loyd R. O. P. et al., 2016, ApJ, 824, 102
Luhar A. K., Galbally I. E., Woodhouse M. T., Abraham N. L., 2021, Atmos. Chem. Phys., 21, 7053
Luther F. M., Wuebbles D. J., Chang J. S., 1977, J. Geophys. Res. (1896–1977), 82, 4935
Lyons T. W., Reinhard C. T., Planavsky N. J., 2014, Nature, 506, 307
May E. M., Taylor J., Komacek T. D., Line M. R., Parmentier V., 2021, ApJ, 911, L30
Mayne N. J., Baraffe I., Acreman D. M., Smith C., Wood N., Amundsen D. S., Thuburn J., Jackson D. R., 2014a, Geosci. Model Dev., 7, 3059
Mayne N. J. et al., 2014b, A&A, 561, A1
Mayne N. J. et al., 2017, A&A, 604, A79
Merlis T. M., Schneider T., 2010, J. Adv. Modeling Earth Syst., 2, 13
Met Office, 2022, Iris: A Python Library for Analysing and Visualising Meteorological and Oceanographic Data Sets, http://scitools.org.uk/
Morgenstern O., Braesicke P., O'Connor F. M., Bushell A. C., Johnson C. E., Osprey S. M., Pyle J. A., 2009, Geosci. Model Dev., 2, 43
Neu J. L., Prather M. J., Penner J. E., 2007, J. Geophys. Res. Atmos., 112
Nixon M. C., Madhusudhan N., 2022, ApJ, 935, 73
Noda S. et al., 2017, Icarus, 282, 1
O'Connor F. M. et al., 2014, Geosci. Model Dev., 7, 41
Parmentier V., Showman A. P., Lian Y., 2013, A&A, 558, A91
Pluriel W., 2023, Remote Sens., 15, 635
Price C., Rind D., 1992, J. Geophys. Res. Atmos., 97, 9919
Proedrou E., Hocke K., 2016, Earth Planets Space, 68, 96
Quanz S. P. et al., 2022, A&A, 664, A21
Renaud J. P., Henning W. G., Saxena P., Neveu M., Bagheri A., Mandell A., Hurford T., 2021, Planet. Sci. J., 2, 4
Ribas I., Gregg M. D., Boyajian T. S., Bolmont E., 2017, A&A, 603, A58
Ridgway R. J. et al., 2023, MNRAS, 518, 2472
Scheucher M., Grenfell J. L., Wunderlich F., Godolt M., Schreier F., Rauer H., 2018, ApJ, 863, 6
Schlichting H. E., Mukhopadhyay S., 2018, Space Sci. Rev., 214, 34
Schubert W. H., Rozoff C. M., Vigh J. L., McNoldy B. D., Kossin J. P., 2007, Q. J. R. Meteorolog. Soc., 133, 595
Segura A., Walkowicz L. M., Meadows V., Kasting J., Hawley S., 2010, Astrobiology, 10, 751
Selsis F., Kasting J. F., Levrard B., Paillet J., Ribas I., Delfosse X., 2007, A&A, 476, 1373

Sergeev D. E., Zamyatina M., 2022, aeolus, https://doi.org/10.5281/zenodo.5145604
Sergeev D. E., Lambert F. H., Mayne N. J., Boutle I. A., Manners J., Kohary K., 2020, ApJ, 894, 84
Sergeev D. E. et al., 2022a, Planet. Sci. J., 3, 212
Sergeev D. E., Lewis N. T., Lambert F. H., Mayne N. J., Boutle I. A., Manners J., Kohary K., 2022b, Planet. Sci. J., 3, 214
Shields A. L., Ballard S., Johnson J. A., 2016, Phys. Rep., 663, 1
Shine K. P. et al., 2003, Q. J. R. Meteorolog. Soc., 129, 1565
Showman A. P., Polvani L. M., 2010, Geophys. Res. Lett., 37, 18
Showman A. P., Polvani L. M., 2011, ApJ, 738, 71
Showman A. P., Wordsworth R. D., Merlis T. M., Kaspi Y., 2013, Comparative Climatology of Terrestrial Planets, Vol. 1. Univ. Arizona Press, Tucson, AZ, https://muse.jhu.edu/chapter/1207491
Steinrueck M. E., Showman A. P., Lavvas P., Koskinen T., Tan X., Zhang X., 2021, MNRAS, 504, 2783
Telford P. J. et al., 2013, .Geosci. Model Dev., 6, 161
Turbet M., Leconte J., Selsis F., Bolmont E., Forget F., Ribas I., Raymond S. N., Anglada-Escudé G., 2016, A&A, 596, A112
Turbet M. et al., 2022, Planet. Sci. J., 3, 211
Vallis G. K., 2017, Atmospheric and Oceanic Fluid Dynamics. Cambridge Univ. Press, Cambridge
Villanueva G. L., Smith M. D., Protopapa S., Faggi S., Mandell A. M., 2018, J. Quantum Spectrosc. Radiat. Transfer, 217, 86
Villanueva G. L., Liuzzi G., Faggi S., Protopapa S., Kofman V., Fauchez T., Stone S. W., Mandell A. M., 2022, Fundamentals of the Planetary Spectrum Generator, https://psg.gsfc.nasa.gov/help.php#handbook
Walters D. et al., 2019, Geosci. Model Dev., 12, 1909
Wang S., Yang J., 2022, Planet. Sci. J., 3, 171
Wild O., Zhu X., Prather M. J., 2000, J. Atmos. Chem., 37, 245
Wilson D. R., Bushell A. C., Kerr-Munslow A. M., Price J. D., Morcrette C. J., 2008, Q. J. R. Meteorolog. Soc., 134, 2093
Wood N. et al., 2014, Q. J. R. Meteorolog. Soc., 140, 1505
Yates J. S., Palmer P. I., Manners J., Boutle I., Kohary K., Mayne N., Abraham L., 2020, MNRAS, 492, 1691
Youngblood A. et al., 2016, ApJ, 824, 101
Zamyatina M. et al., 2023, MNRAS, 519, 3129

This paper has been typeset from a TEX/LATEX file prepared by the author.